Isotope production in proton-, deuteron-, and carbon-induced reactions on ^{93}Nb at 113 MeV/nucleon

Keita Nakano,[1,2,*] Yukinobu Watanabe,[1] Shoichiro Kawase,[1] He Wang,[2] Hideaki Otsu,[2] Hiroyoshi Sakurai,[2] Satoshi Takeuchi,[3] Yasuhiro Togano,[3] Takashi Nakamura,[3] Yukie Maeda,[4] Deuk Soon Ahn,[2] Masayuki Aikawa,[5] Shouhei Araki,[1,2] Sidong Chen,[2] Nobuyuki Chiga,[2] Pieter Doornenbal,[2] Naoki Fukuda,[2] Takashi Ichihara,[2] Tadaaki Isobe,[2] Shunsuke Kawakami,[2,4] Tadahiro Kin,[1] Yosuke Kondo,[3] Shunpei Koyama,[6] Toshiyuki Kubo,[2] Shigeru Kubono,[2] Meiko Uesaka,[2] Ayano Makinaga,[7,8] Masafumi Matsushita,[9] Teiichiro Matsuzaki,[2] Shin'ichiro Michimasa,[9] Satoru Momiyama,[6] Shunsuke Nagamine,[6] Megumi Niikura,[6] Tomoyuki Ozaki,[3] Atsumi Saito,[3] Takeshi Saito,[6] Yoshiaki Shiga,[10] Mizuki Shikata,[3] Yohei Shimizu,[2] Susumu Shimoura,[9] Toshiyuki Sumikama,[2] Pär-Anders Söderström,[2] Hiroshi Suzuki,[2] Hiroyuki Takeda,[2] Ryo Taniuchi,[6] Jun'ichi Tsubota,[3] Yasushi Watanabe,[2] Kathrin Wimmer,[2,6,9] Tatsuya Yamamoto,[2,4] and Koichi Yoshida[2]

[1]*Department of Advanced Energy Engineering Sciences, Kyushu University, 6-1 Kasuga-koen, Kasuga, Fukuoka 816-8580, Japan*
[2]*RIKEN Nishina Center, 2-1 Hirosawa, Wako, Saitama 351-0198, Japan*
[3]*Department of Physics, Tokyo Institute of Technology, 2-12-1 Ookayama, Meguro, Tokyo 152-8551, Japan*
[4]*Faculty of Engineering, University of Miyazaki, 1-1 Gakuen Kibanadai-nishi, Miyazaki, Miyazaki 889-2192, Japan*
[5]*Faculty of Science, Hokkaido University, Kita-10 Nishi-8, Kita-ku, Sapporo, Hokkaido 060-0810, Japan*
[6]*Department of Physics, University of Tokyo, 7-3-1 Hongo, Bunkyo, Tokyo 113-0033, Japan*
[7]*Graduate School of Medicine, Hokkaido University, Kita-15 Nishi-7, Kita-ku, Sapporo, Hokkaido 060-8638, Japan*
[8]*JEin Institute for Fundamental Science, NPO Einstein, 5-14 Yoshida-honmachi, Saikyo, Kyoto 606-8317, Japan*
[9]*Center for Nuclear Study, University of Tokyo, 2-1 Hirosawa, Wako, Saitama 351-0198, Japan*
[10]*Department of Physics, Rikkyo University, 3-34-1 Nishi-Ikebukuro, Toshima, Tokyo 172-8501, Japan*

(Received 18 June 2019; published 8 October 2019)

Isotope-production cross sections for p-, d-, and C-induced spallation reactions on ^{93}Nb at 113 MeV/nucleon were measured using the inverse-kinematics method employing secondary targets of CH_2, CD_2, and C. The measured cross sections for ^{90}Mo, ^{90}Nb, ^{86,88}Y produced by p-induced reactions were found to be consistent with those measured by the conventional activation method. We performed benchmark tests of the reaction models INCL-4.6, JQMD, and JQMD-2.0 implemented in the Particle and Heavy Ion Transport code System (PHITS) and of the nuclear data libraries JENDL-4.0/HE, TENDL-2017, and ENDF/B-VIII.0. The model calculations also showed generally good agreement with the measured isotope-production cross sections for p-, d-, and C-induced reactions. It also turns out that, among the three nuclear data libraries, JENDL-4.0/HE provides the best agreement with the measured data for the p-induced reactions. We compared the present ^{93}Nb data with the ^{93}Zr data, that were measured previously by the same inverse kinematics method (Kawase *et al.*, Prog. Theor. Exp. Phys. **2017**, 093D03 (2017)), with particular attention to the effect of neutron-shell closure on isotope production in p- and d-induced spallation reactions. The isotopic distributions of the measured production cross sections in the ^{93}Zr data showed noticeable jumps at neutron number $N = 50$ in the isotopic chains of $\Delta Z = 0$ and -1, whereas no such jump appeared in isotopic chain of $\Delta Z = 0$ in the ^{93}Nb data. From INCL-4.6 + GEM calculations, we found that the jump formed in the evaporation process is smeared out by the intranuclear cascade component in ^{91}Nb produced by the ^{93}Nb$(p, p2n)$ and $(d, d2n)$ reactions on ^{93}Nb. Moreover, for ^{93}Nb, the distribution of the element-production cross sections as a function of the change in proton number ΔZ is shifted to smaller ΔZ than for ^{93}Zr, because the excited Nb prefragments generated by the cascade process are more likely to emit protons than the excited Zr prefragments, due to the smaller proton-separation energies of the Nb isotopes.

DOI: 10.1103/PhysRevC.100.044605

I. INTRODUCTION

Spallation reactions play key roles in fields of various applications, e.g., radioactive isotope (RI) beam production [1], accelerator-driven transmutation systems [2], and spallation neutron sources for materials science [3]. Over the past few decades, numerous studies have been devoted to spallation reactions in order to understand their mechanisms and to accumulate fundamental data for such applications [4–11]. The study of spallation reactions thus remains of interest from the point of view of fundamental physics as well as for applications.

*knakano@aees.kyushu-u.ac.jp

Recently, isotope-production cross sections for p- and d-induced spallation reactions on the long-lived fission products (LLFPs) ^{93}Zr at 105 MeV/nucleon [12] and ^{107}Pd at 118 and 196 MeV/nucleon [13] were measured using the inverse-kinematics method at the RIKEN RI Beam Factory (RIBF) in order to accumulate the basic data necessary for nuclear-waste transmutation. From comparisons among the measured data, noticeable jumps were observed in the ^{93}Zr data for the isotopic distributions of the measured cross sections for the production of Zr and Y chains due to the shell effect at neutron magic number $N = 50$. This experimental result suggests the importance of shell closure in the description of p- and d-induced spallation reactions on target nuclei near this magic number. It is worth emphasizing that the production cross sections for stable residual nuclei such as ^{90,91,92}Zr in the isotopic chain of Zr cannot be measured by the conventional activation method. The inverse-kinematics method thus has a great advantage for systematic measurements of the isotopic distributions of production cross sections. Similar experimental data for nuclei adjacent to ^{93}Zr are required to confirm the effects of neutron-shell closure at $N = 50$ on isotope-production in p- and d-induced spallation reactions.

In the ^{93}Zr experiment, ^{93}Nb, one of the isobars with $A = 93$, constitutes of the secondary beam produced by the in-flight fission of ^{238}U at 345 MeV/nucleon caused by interaction with a beryllium target. The proton and neutron numbers in ^{93}Nb are $Z = 41$ and $N = 52$, respectively, whereas they are $Z = 40$ and $N = 53$ in ^{93}Zr. It is of interest to see how the difference of a single nucleon in the initial proton and neutron numbers influences the isotopic distribution of the measured production cross sections. In addition, there are many experimental data for isotope-production cross sections from the conventional activation method [14], because ^{93}Nb is a stable nucleus comprising 100% of the natural abundance, and nuclear data libraries up to 200 MeV [15–17] are also available. Thus, the new data for ^{93}Nb provide useful checks on the consistency between the isotope-production data measured by the two different methods. Also, the ^{93}Nb data can contribute to the validation of the nuclear data libraries and of the reaction models used in our previous work on ^{93}Zr [12], namely, the Liège Intranuclear Cascade (INCL) model [18] and the generalized evaporation model (GEM) [19] employed in the Particle and Heavy Ion Transport code System (PHITS) [20,21]. Moreover, isotope-production cross sections can be extracted for the ^{93}Nb + C reaction because carbon was used as a reaction target in the inverse-kinematics experiment [12]. The new data on the ^{93}Nb + C reaction can be used to benchmark the JAERI Quantum Molecular Dynamics (JQMD) code [22,23] implemented in PHITS, which is employed to describe the fragmentation reactions induced by heavy ions.

In Sec. II, the experimental procedure is described. Sec. III is devoted to data analysis, including the method of particle identification, correction for charge-state changes, and the estimation of systematic errors. In Sec. IV, the measured data are compared with existing activation data, theoretical model calculations, and nuclear data libraries. Then, comparisons with the previous ^{93}Zr data are shown, devoting particular attention to the effects of shell closure on isotope production. Finally, a summary and our present conclusions are described in Sec. V.

II. EXPERIMENT

The experiment was carried out at the RIKEN RIBF. The BigRIPS RI beam separator and the ZeroDegree Spectrometer (ZDS) were used to analyze the incident ^{93}Nb beam and the reaction products [24], respectively.

The experimental procedure was the same as reported in Ref. [12]. In the present experiment, a ^{238}U primary beam accelerated up to 345 MeV/nucleon impinged onto 3-mm-thick ^{9}Be production target installed at the entrance of BigRIPS. The secondary beam containing ^{93}Nb and ^{93}Zr ions was produced through in-flight fission of the ^{238}U primary beam. The typical current of the primary beam was approximately 4 enA. In the first half of BigRIPS, the secondary beam was purified by using 5-mm- and 3.5-mm-thick, wedge-shaped, aluminum degraders and slits. The momentum acceptance of BigRIPS was set to be $\pm 1\%$ by the slit at the momentum-dispersive focal plane. In the second half of BigRIPS, the particle identification of the secondary beam was performed event-by-event using the TOF-$B\rho$-ΔE method [25], employing plastic scintillators, double parallel-plate avalanche counters (PPACs), and multisampling ionization chambers (MUSICs) as beamline detectors. Then the secondary beam impinged onto the secondary targets CH_2 (179.2 mg/cm^2), CD_2 (217.8 mg/cm^2), and C (226.0 mg/cm^2) located at the entrance of the ZDS. The average intensity of the ^{93}Nb beam was approximately 70 counts per second (cps), with 4.4% purity in front of the secondary target. The beam energy was 113 MeV/nucleon at the center of the secondary targets. The residual nuclei produced by nuclear reactions with the secondary targets were also identified event by event using the TOF-$B\rho$-ΔE method. The momentum acceptance of ZDS is limited to less than $\pm 3\%$. Five different magnetic field settings, $\Delta(B\rho)/B\rho = -9\%$, -6%, -3%, 0%, and $+3\%$ were adopted in order to measure the wide range of mass numbers of reaction products. Note that a $B\rho$ setting of 0% corresponds to the magnetic rigidity of the ^{93}Zr beam. An empty-frame run was also performed in order to subtract background events from beamline materials.

III. DATA ANALYSIS

A. Identification of the secondary beam

As mentioned above, particle identification of the secondary beam was performed using the TOF-$B\rho$-ΔE method [25]. In the present work, the atomic number Z and the mass-to-charge ratio A/Q were deduced from time-of-flight (TOF) measured by the plastic scintillators, magnetic rigidity ($B\rho$) measured by the PPACs, and energy loss (ΔE) measured by the MUSICs with the following equations:

$$\mathrm{TOF} = \frac{L}{\beta c}, \tag{1}$$

$$\frac{A}{Q} = \frac{B\rho}{\beta\gamma}\frac{c}{m_u}, \tag{2}$$

$$\frac{dE}{dx} = \frac{4\pi e^4 Z^2}{m_e v^2} N_Z \left[\ln\frac{2m_e v^2}{I} - \ln(1-\beta^2) - \beta^2\right], \tag{3}$$

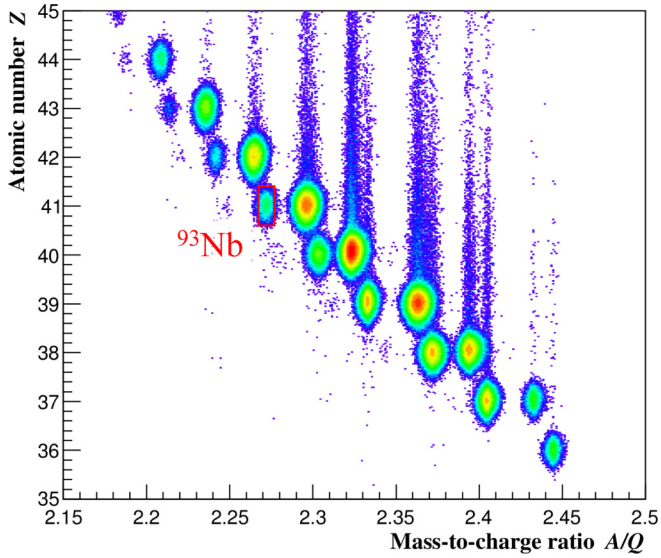

FIG. 1. Particle identification plot for the secondary beam. The red box outlines the selected ^{93}Nb events.

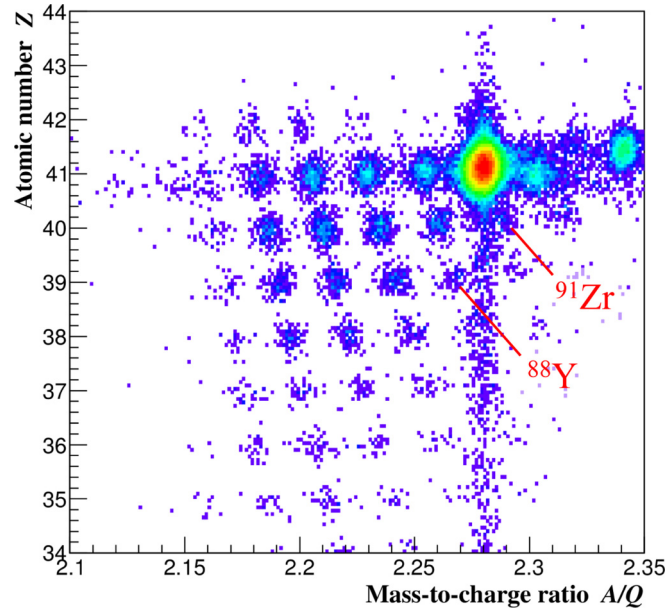

FIG. 2. Particle identification plot for the reaction products from the CH_2 target with the 0% $B\rho$ setting after selecting the ^{93}Nb beam.

where L is the flight path length, m_u the atomic mass unit, m_e the electron mass, e the electron charge, and c the velocity of light. The variable v is the velocity of the projectile in the secondary beam, and β and γ are the corresponding relativistic velocity and Lorents factor, respectively. Also, N, z, and I indicate the atomic density, the atomic number, and the mean excitation potential of the material, respectively. Two characteristic gamma rays with energies of 315 and 492 keV from ^{92m}Y [26] were used for the isomer tagging [27,28] to determine the absolute Z and A/Q. Figure 1 shows the particle identification plot for the secondary beam. The vertical and horizontal axes correspond to Z and A/Q, respectively. The resolution of 0.40 (FWHM) in Z and 0.23 (FWHM) in A is clearly sufficient to identify the ^{93}Nb beam. Although the beam tails along the y axis that result from signal pileup in MUSIC are observed, there is no contamination in the ^{93}Nb beam. Moreover, the contribution of the isomer state ^{93m}Nb ($E_x = 0.0308$ MeV, $T_{1/2} = 16.12$ years), which is included in the identified ^{93}Nb beam, is estimated to be negligible based on an optical model calculation with the CCONE code [29]. The events in the ranges $40.6 \leqslant Z \leqslant 41.4$ and $2.266 \leqslant A/Q \leqslant 2.276$ were selected as ^{93}Nb, as shown by the red box in Fig. 1. The energy of the ^{93}Nb beam was determined to be 113 MeV/nucleon with the energy spread of ±11 MeV/nucleon in the secondary targets, based on beam simulations using the LISE++ code [30]. The specific energy spread of the secondary beam was ±0.36%, which is negligible compared with the energy spread in the secondary targets.

B. Identification of reaction products

Particle identifications of the reaction products was performed in almost the same way as for the secondary beam. Figure 2 shows the particle identification plot for reaction products from the CH_2 target with the 0% $B\rho$ setting after selecting the ^{93}Nb beam. The resolution for ^{90}Nb was 0.53 (FWHM) in Z and 0.26 (FWHM) in A, and individual reaction products are identified unambiguously. Many events located at $Z \simeq 41$ and $A/Q \simeq 2.283$ correspond to the incident ^{93}Nb beam passing through without changing A or Z.

C. Correction for charge-state changes

The secondary beam and the reaction products were mostly in fully stripped (F.S.) states, for which the charge is proportional to eZ. However, the charge states can change by picking up or losing electrons while passing through the beamline materials. Charge-state-changing events that produce hydrogen-like (H-like) or helium-like (He-like) particles before the final focal plane of BigRIPS were removed automatically by selecting the ^{93}Nb beam in Fig. 1. On the other hand, such charge-state-changing events also need to be eliminated in the ZDS. Figure 3 shows the charge-state distribution in the ZDS after selecting the ^{93}Nb beam. The vertical and horizontal axes correspond to the horizontal positions at the intermediate dispersive and final achromatic focal planes, respectively. Each locus corresponds to the charge state in the first and second half of the ZDS; the vertical axis represents the charge state in the first half, whereas the horizontal axis corresponds to the difference in the charge state between the first and second half of the ZDS. The locus in the upper center corresponds to fully stripped events in both sections (F.S. → F.S.), and the loci at opposite sides of the horizontal axis represent charge-state-changing events at the intermediate focal plane, i.e., fully stripped to hydrogenlike (F.S. → H-like) at the right side and hydrogenlike to fully stripped (H-like → F.S.) events at the left side. The locus located at the lower center is equivalent to hydrogen-like events in the whole ZDS (H-like → H-like). These charge-state-changing events were removed because it can be assumed that the charge state does not change at the intermediate focal plane, as noted in [25]. The yields of the removed charge-state-changing events were compensated by

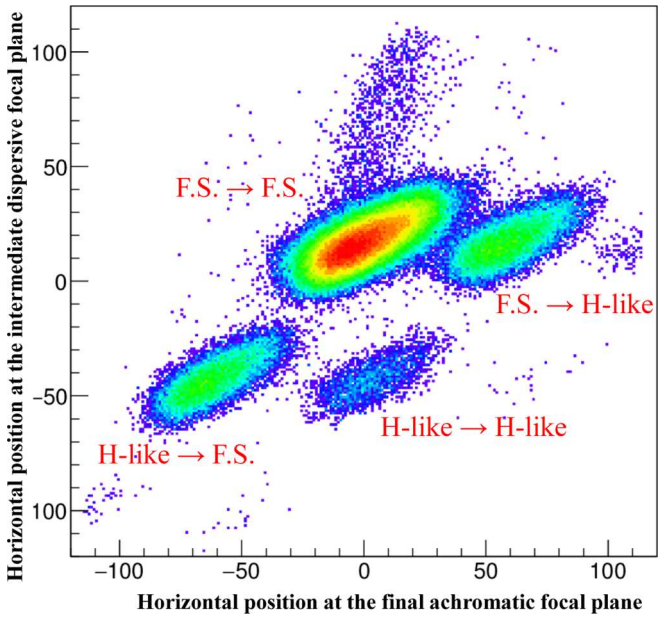

FIG. 3. Charge state distribution in the ZDS given by the horizontal positions at the intermediate dispersive and final achromatic focal planes for the CH_2 target and the $+3\%$ $B\rho$ setting, after selecting the ^{93}Nb beam.

using the ratio of the F.S. events in the whole ZDS to the total events calculated by the LISE++ code [30].

D. Isotope-production cross-sections

Isotope-production cross-sections for p- and d-induced reactions were derived by subtracting the background contribution of the beamline materials and the carbon target from the yields measured in the CH_2 and CD_2 target runs, respectively. From the individual ZDS $B\rho$ settings, the p-induced cross section σ_p is given by

$$\sigma_p = \frac{1}{2}\left[\frac{1}{t_{CH_2}}\left(\frac{Y_{CH_2}}{c_{CH_2}B_{CH_2}} - \frac{Y_{emp}}{c_{emp}B_{emp}}\right) - \frac{1}{t_C}\left(\frac{Y_C}{c_C B_C} - \frac{Y_{emp}}{c_{emp}B_{emp}}\right)\right], \quad (4)$$

where B is the number of incident ^{93}Nb ions, Y is the number of detected reaction products, and t is the areal density of the reaction targets. The parameter c corresponds to the correction factor for charge-state-changes. The subscripts CH_2, C, and emp denote individual runs with the CH_2, C, and empty-frame targets, respectively. For the d-induced case, the subscript CH_2 is replaced by CD_2. Isotope-production cross section for C-induced reactions was derived by subtracting the contribution of the beamline materials from the C target run using the following equation:

$$\sigma_C = \frac{1}{t_C}\left(\frac{Y_C}{c_C B_C} - \frac{Y_{emp}}{c_{emp}B_{emp}}\right). \quad (5)$$

Final isotope-production cross sections were determined as weighted means of the cross sections measured for different ZDS $B\rho$ settings, with the weights given by the statistical errors.

E. Systematic error evaluation

The systematic errors in the measured production cross sections are composed of two major components: the uncertainty in the areal density of the reaction targets and the correction factor c in Eq. (4) for the charge-state changes. The former were estimated to be less than 2% in Ref. [31], and the latter was estimated to be less than 1% from the comparisons between the experimental and calculated correction factors for the charge-state changing.

IV. RESULTS AND DISCUSSION

First, the isotope-production cross sections measured for the p-, d-, and C-induced reactions on ^{93}Nb are presented and comparison is made among them. Then, the present data for the p-induced reactions are compared with past data measured by the activation method [14] to check the consistency between the data measured by the inverse-kinematics and activation methods. In addition, benchmark tests of theoretical model calculations and nuclear data libraries are performed using our measured isotope-production cross sections. Finally, comparisons between the ^{93}Nb data and the previously measured ^{93}Zr data [12] are discussed, with a focus on the effects of shell closure on isotope production in p- and d-induced spallation reactions.

A. Experimental isotope-production cross sections

Figure 4 shows the isotope-production cross sections for p-, d-, and C-induced reactions on ^{93}Nb at the energy of 113 MeV/nucleon using the inverse-kinematics method. The error bars include only the statistical uncertainties. The experimental results demonstrate the advantage of the inverse-kinematics method, with which one can measure isotope-production cross sections over a wide range of isotopic chains, including stable isotopes.

As shown in panel (a), σ_p for the Mo isotopes for which the atomic number is increased by 1 ($\Delta Z = +1$) from the projectile ^{93}Nb is approximately twice as large as σ_d. A similar tendency is observed in the production of isotopes with $\Delta Z = +1$ in other studies [12,13,31,32]. From the Nb isotopes (b) to the Rb isotopes (f), σ_p decreases more rapidly with decreasing atomic number than σ_d and σ_C, resulting in σ_p being smaller than σ_d and σ_C for the Y, Sr, and Rb isotopes. This can be explained by the difference in the excitation energies of the prefragments formed by the intranuclear cascade process. The incident energy per nucleon is the same for three targets, but the total incident energies of the d- and C-induced reactions are higher than for the p-induced reactions. Thus, it is expected that prefragments with higher excitation energies are formed in the d- and C-induced reactions than in the p-induced reactions, and the production yields of isotopes with lower Z are enhanced by the sequential decays of more nucleons than in the p-induced reactions.

In Fig. 4, the discontinuity in production cross sections for p-, d-, and C-induced reactions is observed between ^{90}Zr and ^{91}Zr because of the closed-shell structure at the neutron

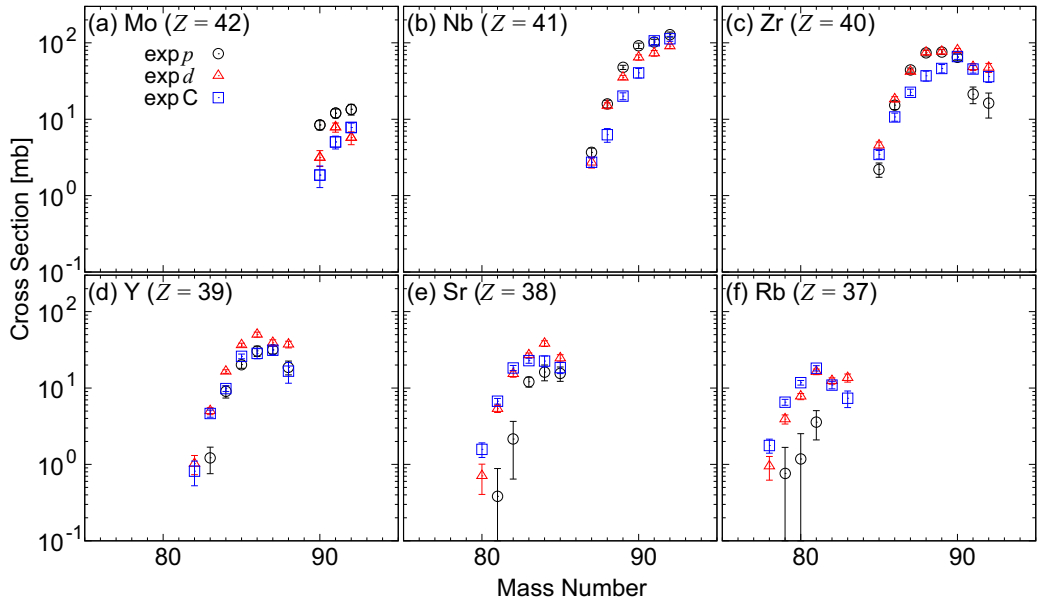

FIG. 4. Measured isotope-production cross sections for ^{93}Nb + p, d, and C reactions at 113 MeV/nucleon: (a) Mo, (b) Nb, (c) Zr, (d) Y, (e) Sr, and (f) Rb. The black circles, red triangles, and blue squares represent the production cross sections for the p-induced reactions (σ_p), the d-induced reactions (σ_d), and the C-induced reaction (σ_C), respectively.

magic number $N = 50$. The neutron separation energies S_n are 8634.78 keV for ^{92}Zr, 7194.35 keV for ^{91}Zr, 11968 keV for ^{90}Zr, and 9318 keV for ^{89}Zr [33]. Thus, ^{91}Zr emits a neutron more easily than the other Zr isotopes. The production of ^{90}Zr therefore increases relative to ^{91}Zr. These discontinuous jumps are weakened for the heavier incident particles, because the larger excitation energies of the prefragments probably allow them to compensate for the effect of shell structure. Although a jump was observed in the Zr isotopes ($\Delta Z = 0$) in the ^{93}Zr data [12], no jump appeared in the Nb isotopes ($\Delta Z = 0$) in the ^{93}Nb data, despite the large gap in S_n between ^{92}Nb (S_n = 7887 keV) and ^{91}Nb (S_n = 12048 keV). We discuss this difference in the context of a theoretical model calculation in Sec. IV D

B. Comparison with the activation data

Several isotope-production data measured by the conventional activation method have been reported to date for p-induced reactions on ^{93}Nb [14]. The present data measured by the inverse-kinematics method can be compared with the data provided as independent yields from these activation data. Here we chose the four radioactive isotopes ^{90}Mo, ^{90}Nb, ^{88}Y, and ^{86}Y for comparison. The results are shown in Fig. 5. Note that the red horizontal arrows indicate the energy spread in the reaction target. The black squares denote the activation data [14], and the black lines connect these data with cubic spline functions. These figures show that within the experimental errors the data measured by the inverse-kinematics method are consistent with those measured by the activation method.

C. Comparison with model calculations and nuclear data libraries

In this subsection, we perform benchmark tests for the reaction models implemented in PHITS version 3.00 [20,21] and for the nuclear data libraries [15–17] by comparisons with the isotope-production cross-section data measured in the present work. In the PHITS calculations, a spallation reaction is described as a two-step process; that is, prefragments are formed via the intranuclear cascade (INC) process, and the excited prefragments subsequently decay by the evaporation of light particles and gamma rays. The present σ_p and σ_d data are used to benchmark the Liège Intranuclear Cascade

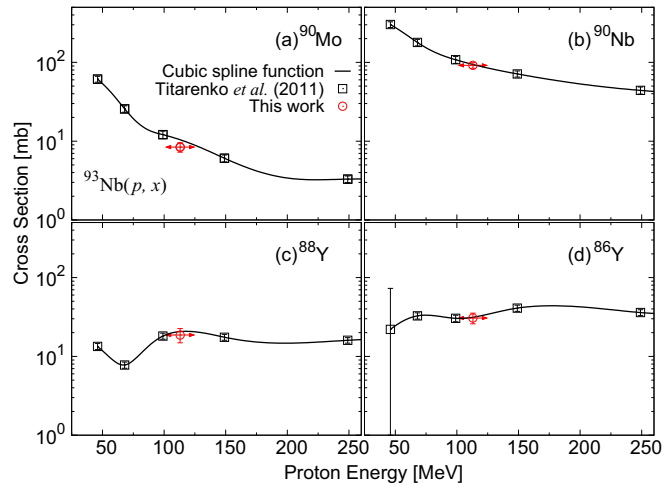

FIG. 5. Comparison between data measured by the inverse-kinematics method and by the activation method [14] for the production cross sections of (a) ^{90}Mo, (b) ^{90}Nb, (c) ^{88}Y, and (d) ^{86}Y. The red circles represent the measured data with the inverse-kinematics method along with the statistical uncertainties, and the red arrows in the x direction correspond to the energy spread at the reaction targets. The black lines connect the activation data denoted by black squares with cubic spline functions.

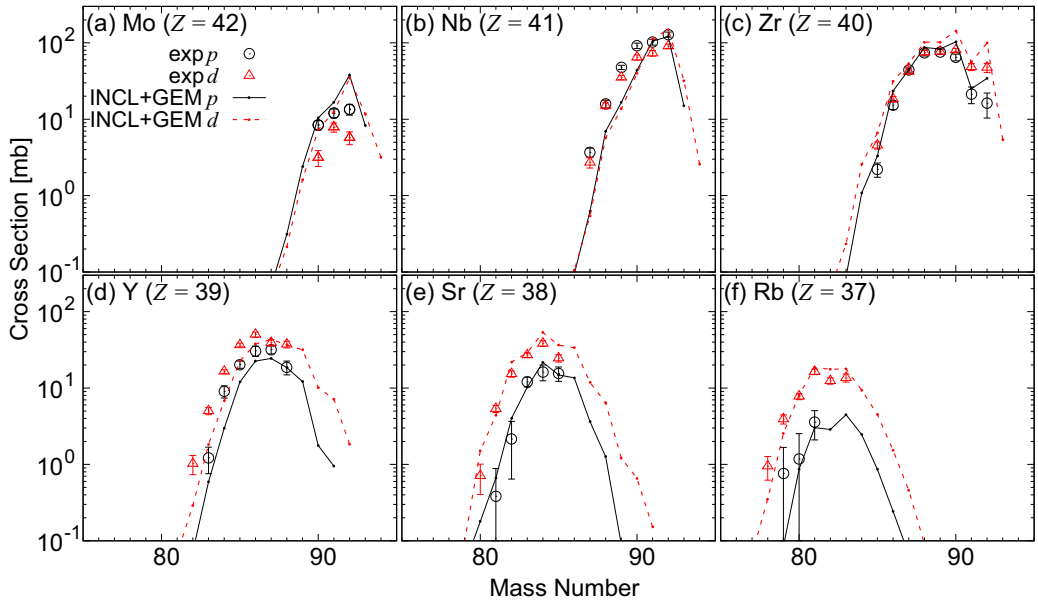

FIG. 6. Comparison between experimental isotope-production cross sections for p- and d-induced reactions on ^{93}Nb at 113 MeV/nucleon and PHITS calculations with INCL-4.6 + GEM.

(INCL-4.6) model [18] for the INC process and the generalized evaporation model (GEM) [19] for the evaporation process. In addition, the experimental σ_p data are compared with the data stored in the latest nuclear data libraries, i.e., JENDL-4.0/HE [15], TENDL-2017 [16], and ENDF/B-VIII.0 [17]. Among these libraries, TENDL-2017 contains the σ_d data, but the maximum incident energy of 200 MeV is less than the total incident energy of 226 MeV in the present measurements. Therefore, the experimental σ_d data are not compared with the TENDL-2017 data. The σ_C data are compared with model calculations using JQMD [22] and JQMD-2.0 [23], where JQMD-2.0 is a modified version of JQMD that was implemented in PHITS to improve the treatment of peripheral collisions by considering the relativistic covariance of the Hamiltonian and modifying the treatment of neutron-proton scattering near the nuclear surface. PHITS has a number of options for the total reaction cross sections: it employs the Pearlstein-Niita formula [34] for p-induced reactions and the KUROTAMA model [35,36] for the d- and C-induced reactions in the present work.

1. Proton- and deuteron-induced reactions

Figure 6 compares our experimental σ_p and σ_d data with calculations that use INCL-4.6 plus GEM as implemented in the PHITS. The black circles and red triangles denote the experimental σ_p and σ_d data, respectively, and the black solid and red dashed lines represent the corresponding theoretical calculations.

The calculations are in overall agreement with the experimental data. The χ^2 values are 13.1 for the p-induced reactions and 51.5 for the d-induced reactions. The latter is approximately four times worse than the former because the production cross sections for isotopes near the target nucleus ^{93}Nb are significantly overestimated for the d-induced reactions. The jumps in the production cross sections at the neutron magic number 50 for the Zr isotopes are reproduced reasonably well in panel (c), whereas neither the calculation nor the measured cross section show a jump at the neutron magic number for the Nb isotopes in panel (b). The effects of shell closure on isotope production will be discussed together with the data on the ^{93}Zr + p and d reactions [12] in Sec. IV D.

There are two major discrepancies between the experimental data and the PHITS calculations in Fig. 6. First, the calculations overestimate the production cross sections of isotopes near the target nucleus, such as ^{92}Mo and ^{92}Zr. The similar overestimation was observed in our previous data on the ^{93}Zr + p and d reactions [12]. The INC process described by the INCL-4.6 model dominates in the formation of these isotopes, as we show below in Sec. IV D. As discussed in Refs. [12,37,38], one reason for the overestimations is that the INCL-4.6 model fails to reproduce the excitation energy distributions in the prefragments formed after the INC process. If the transition to highly excited states in the prefragments is enhanced, the production of ^{92}Mo and ^{92}Zr is expected to be reduced, because more nucleons can be emitted from the prefragments via the evaporation process. Second, the even-odd staggering in the calculated results, shown clearly in Fig. 6(e), is not appreciable in the experimental data. A similar situation was also pointed out in Refs. [12,31]. The exaggerated even-odd staggering may be caused by the absence of competition between particle and γ-ray emissions in the evaporation process or by inappropriate pairing corrections in the level densities employed in GEM in the PHITS calculations [31].

In Fig. 7, the isotope-production cross sections taken from JENDL-4.0/HE, TENDL-2017, and ENDF/B-VIII.0 are plotted together with the measured data. The χ^2 values are 6.92 for JENDL-4.0/HE, 12.11 for TENDL-2017,

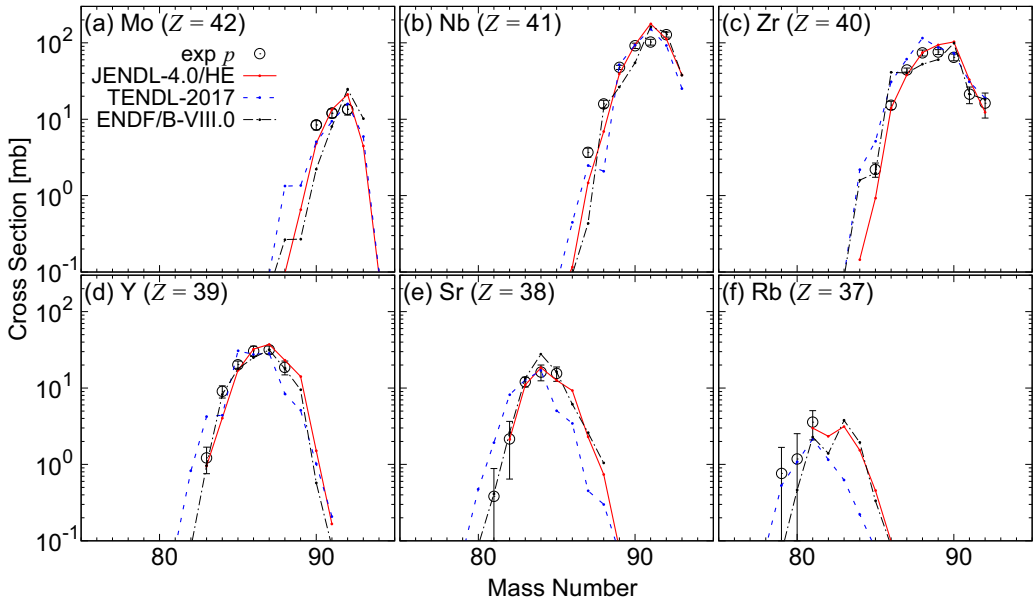

FIG. 7. Comparison of experimental isotope-production cross sections for p-induced reactions on ^{93}Nb at 113 MeV with three nuclear data libraries: JENDL-4.0/HE (solid), TENDL-2017 (dashed), and ENDF/B-VIII.0 (dash-dotted).

and 13.29 for ENDF/B-VIII.0. The JENDL-4.0/HE cross sections shows fairly good agreement with the measured data, resulting in the smallest χ^2 value among all the nuclear data libraries even smaller than for the PHITS calculations, although there are no data in the low-mass-number regions for the Sr and Rb isotopes. There are three major discrepancies between TENDL-2017 and the experimental data: the peak seen in ^{91}Nb; the overestimates seen in the even-Z isotopes, i.e., Zr and Sr, in contrast to the INCL-4.6 + GEM calculations and JENDL-4.0/HE; and the strong even-odd staggering seen in all the isotopes. In contrast, ENDF/B-VIII.0 reproduces the isotopic distributions of Y and Sr better than the others, but the even-odd staggering appears strongly in the Zr isotopes, which results in the worst χ^2 value among the three nuclear data libraries.

2. Carbon-induced reactions

Figure 8 shows comparisons between the measured σ_C and PHITS calculations using JQMD + GEM and JQMD-2.0 + GEM. The blue squares, black solid lines, and blue dash-dotted lines correspond to the experimental data, the JQMD + GEM calculations, and JQMD-2.0 + GEM calculations, respectively. The JQMD + GEM results show much smaller production cross sections for the isotopes near ^{93}Nb, because JQMD does not treat peripheral collisions appropriately. These calculations were recently improved by considering the relativistic covariance of the Hamiltonian and by modifying the treatment of neutron-proton scattering near the nuclear surface. The improved version is called JQMD-2.0 [23]. As shown in Fig. 8, the JQMD-2.0 calculations result in a considerable improvement in the underestimation of ^{91,92}Nb, whereas only slight changes appear in the production cross sections of the other isotopes. The productions of ^{91,92}Nb are sensitive to the treatment of neutron-proton scattering near the nuclear surface because peripheral collisions generate the prefragments with low excitation energy, resulting in one- or two-neutron knockout reactions. As a result, the productions of ^{91,92}Nb are enhanced. However, the production cross sections for ^{91,92}Mo are considerably underestimated by both of the calculations. In the calculated isotopic distributions, the strong even-odd staggering is seen in the Zr and Sr isotopes for both the p- and d-induced cases shown in Fig. 6. In addition, the production cross sections for the Nb isotopes are underestimated in the neutron-deficient region, whereas those in the neutron-rich regions of the Y, Sr, and Rb isotopes are overestimated. The disagreement may be due mainly to the modeling in GEM, as for the p- and d-induced reactions. Finally, the χ^2 values are 34.2 for JQMD + GEM and 31.2 for JQMD-2.0 + GEM. The latter is slightly better than the former, thanks to the improvement in the treatment of peripheral collisions in JQMD-2.0.

D. Comparison with ^{93}Zr data

We compare the present ^{93}Nb data and the previous ^{93}Zr data [12], with particular attention to the effect of the neutron-shell closure at $N = 50$ on isotope production. The two nuclei are isobars, with $A = 93$: the proton number is $Z = 41$ and the neutron number is $N = 52$ for ^{93}Nb, whereas they are $Z = 40$ and $N = 53$ for ^{93}Zr. Note that the reaction energies are 113 MeV/nucleon for ^{93}Nb and 105 MeV/nucleon for ^{93}Zr. Since this difference is less than 10%, however, it is expected that its influence is negligible.

The isotopic distributions of the ^{93}Nb and ^{93}Zr data are compared in Fig. 9. Panels (a) and (c) show the isotope-production cross sections for (p, pxn) reactions on ^{93}Nb and ^{93}Zr, respectively, whereas panels (b) and (d) present those for (p, $2pxn$) reactions on ^{93}Nb and ^{93}Zr, respectively. The experimental data are plotted as open circles and triangles

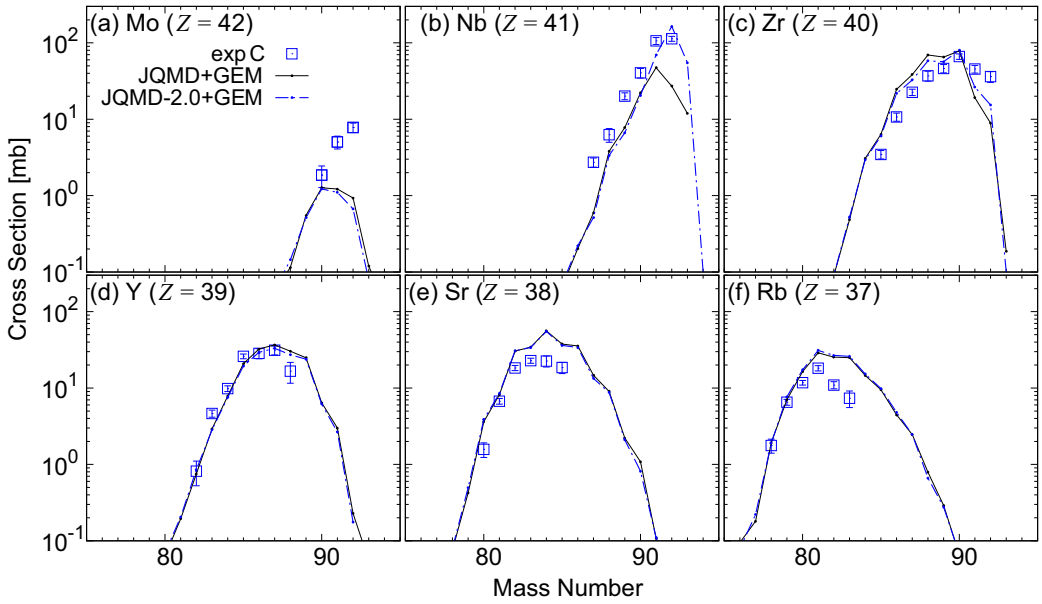

FIG. 8. Comparison of experimental isotope-production cross sections for C-induced reactions on ^{93}Nb at 113 MeV/nucleon and PHITS calculations with JQMD + GEM (solid) and JQMD-2.0 + GEM (dash-dotted).

for the ^{93}Nb and ^{93}Zr data, respectively. We focus on the production of isotopes with the magic number $N = 50$. Jumps are clearly seen at $N = 50$ in the experimental production cross sections for both the $(p, 2pxn)$ results, namely, for ^{90}Zr in panel (b) and ^{89}Y in panel (d). However, such a jump is not observed in the production of ^{91}Nb with $N = 50$ from the

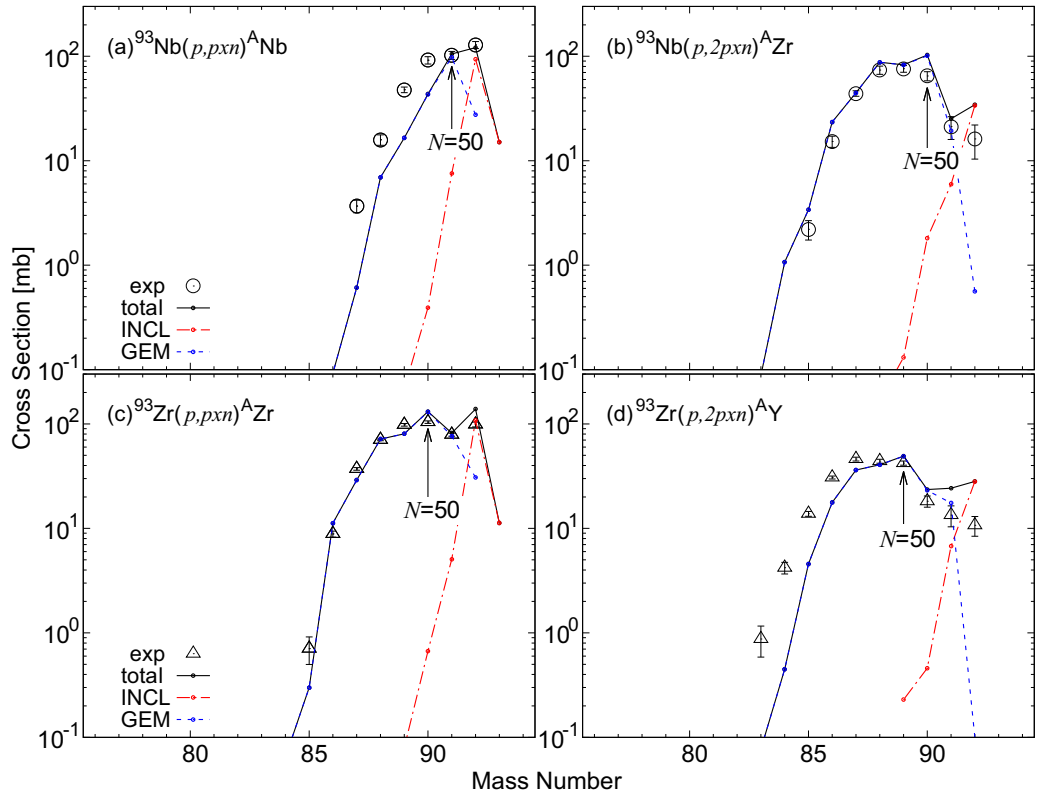

FIG. 9. Isotope-production cross sections for the (p, pxn) and $(p, 2pxn)$ reactions on ^{93}Nb and ^{93}Zr. The calculated results denoted by the black solid lines are decomposed into two components: the production of isotopes via just the INC process described by INCL-4.6 (red dashed-dotted line) and that via the sequential evaporation process described by GEM (blue dashed line).

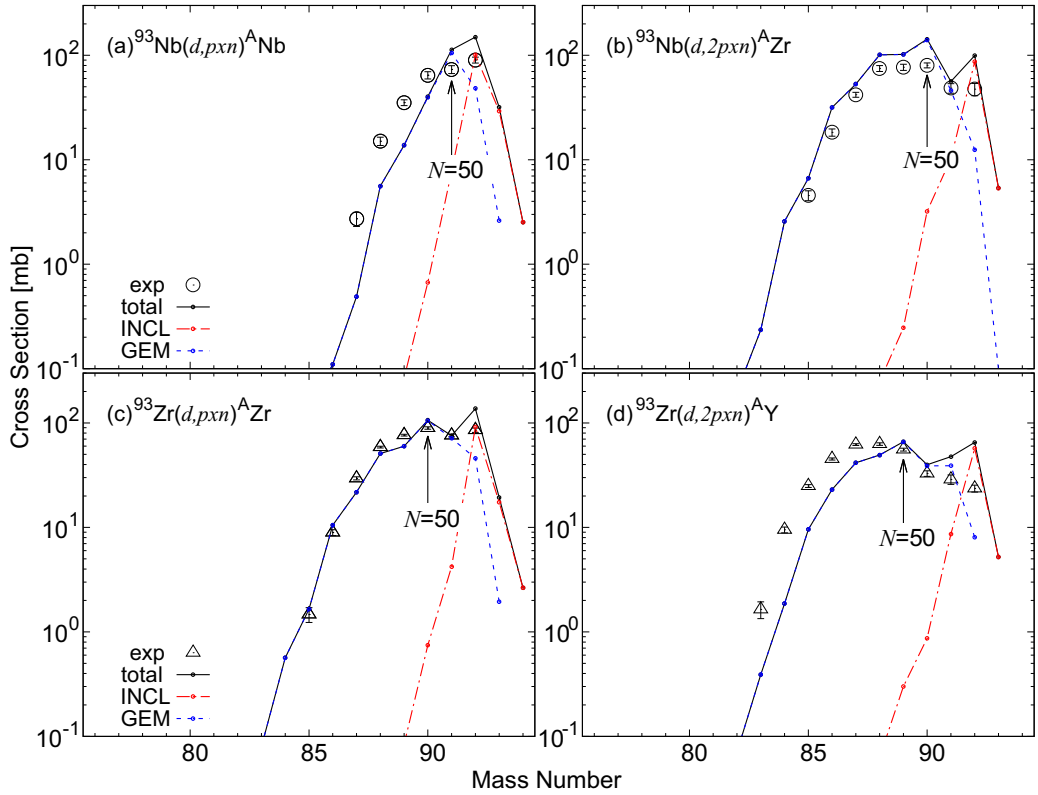

FIG. 10. The same as Fig. 9, but for the (d, pxn) and (d, $2pxn$) reactions on ^{93}Nb and ^{93}Zr.

^{93}Nb(p, pxn) reactions shown in panel (a), whereas a jump does appear at $N = 50$ in the ^{93}Zr(p, pxn) reactions shown in panel (c).

On the basis of a theoretical model calculation, we can now discuss the reason why the jump disappears at $N = 50$ in panel (a). In Fig. 9, the production cross sections calculated with PHITS are decomposed into two components, namely, the INCL and GEM components. The former, shown by the red dash-dotted line, represents the direct production yield via the INC process, i.e., the formation of prefragments having excitation energies lower than the particle-emission threshold energies followed by sequential deexcitation by γ-ray emission. Conversely, the GEM component shown as the blue dashed line corresponds to the production of isotopes by particle evaporation from highly excited prefragments generated after the INC process. The INCL components look similar for both the ^{93}Nb and ^{93}Zr target nuclei, and they have no jump at the magic number $N = 50$, with the maximum values at $A = 92$ corresponding to one-nucleon removal from the target nuclei. In contrast, the GEM component shows a maximum production yield in each isotopic distribution at $N = 50$, and a jump in the production cross section appears in all the panels. When one compares the sum of the INCL and GEM components, which are in reasonable agreement with the measured data, the jump seen at $N = 50$ in the GEM component of the ^{93}Nb(p, pxn) reaction is smeared out by the INCL component and disappears, as shown in panel (a). Thus, it was found that the appearance of the jump in the isotopic distribution depends on the relative fraction of INCL and GEM components in the isotope production. For the other reactions, the INCL components do not disturb the jumps seen in the GEM components, because the mass number corresponding to $N = 50$ occurs far from $A = 92$, where the INCL component provides the maximum value. Thus, the effects of the closed neutron-shell on isotope production appear in all three cases.

Comparisons of the d-induced reactions on ^{93}Nb and ^{93}Zr are shown in Fig. 10. The same result as for the p-induced spallation reaction is obtained, and the effect of neutron-shell closure at $N = 50$ in the d-induced spallation reactions can be interpreted in the same manner as for the p-induced ones.

Finally, the measured element-production cross sections for ^{93}Nb and ^{93}Zr are plotted as a function of the change in atomic number ΔZ by the black circles and the red triangles in Fig. 11 in order to see how the difference of a single nucleon in the initial proton and neutron numbers influences the measured distributions. Panels (a) and (b) present the p- and d-induced reactions, respectively. In panel (a), the ΔZ distribution of the p-induced reactions on ^{93}Zr shows a sharp peak at $\Delta Z = 0$, whereas a broader peak is observed in the ΔZ distribution for ^{93}Nb, resulting in a smaller cross section at $\Delta Z = 0$ and a larger cross section at $\Delta Z = -1$ than in the ^{93}Zr data. This difference in the ΔZ distribution can be explained by the difference in proton and neutron separation energies between the Nb and Zr isotopes. In Fig. 12(a), the calculated branching ratios for the proton and neutron emission from excited Nb and Zr isotopes generated by the INC process at 15, 35, and 55 MeV are shown as black and red

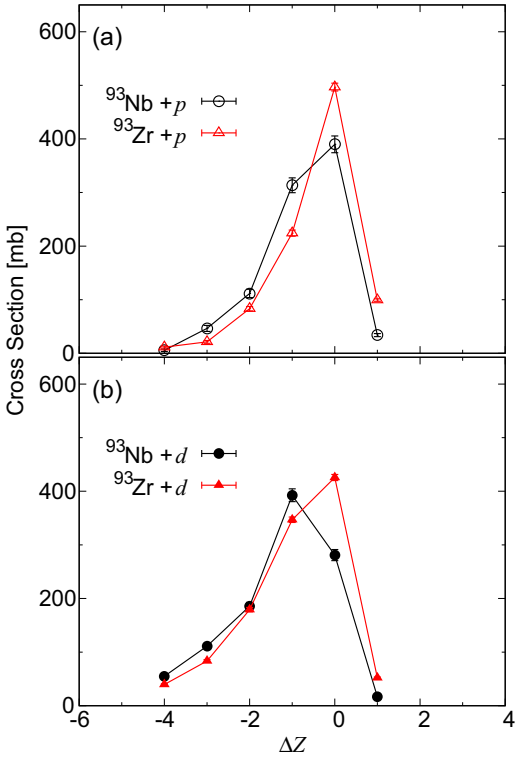

FIG. 11. Distribution of production cross sections as a function of the change in atomic number ΔZ (a) for p-induced reactions on ^{93}Nb and ^{93}Zr and (b) for d-induced reactions.

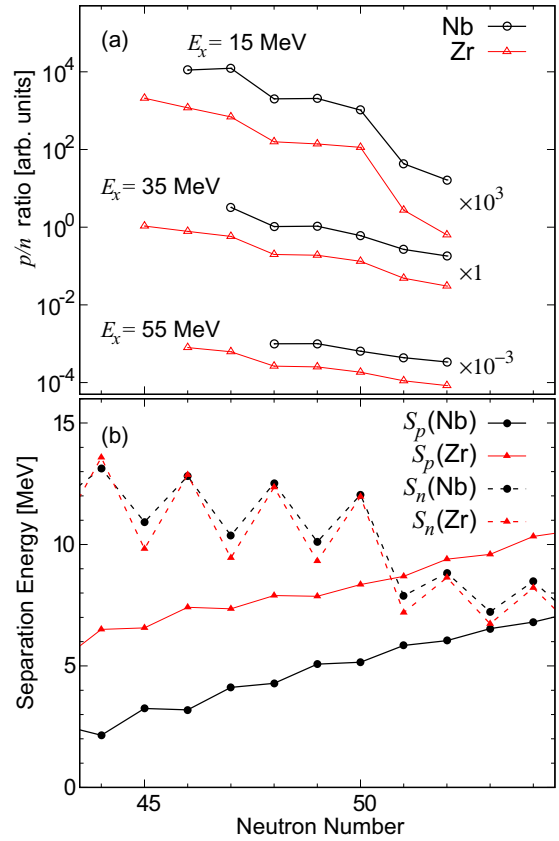

FIG. 12. (a) The branching ratios for proton and neutron emission from excited Nb and Zr isotopes and (b) the separation energies of protons and neutrons from Nb and Zr isotopes, both as a function of neutron number.

lines, respectively. The niobium isotopes have larger proton emission probabilities than the Zr isotopes at all excitation energies. This tendency originates from the proton and neutron separation energies for each isotope. In Fig. 12(b), the separation energies S_p and S_n calculated from the mass table AME2016 [33] are shown as a function of neutron number by the solid and dashed lines, respectively. Both the Nb and Zr isotopes have almost the same S_n, whereas S_p has a gap of approximately 5 MeV because of subshell closure at $Z = 40$. The different behaviors of S_n and S_p enhance the proton emission from each excited Nb prefragment generated by the INC process compared with the Zr isotopes. As a result, it is expected that the ΔZ distribution for ^{93}Nb spreads toward smaller ΔZ.

Figure 11 also compares the change ΔZ produced by p- and d-induced reactions on ^{93}Nb and ^{93}Zr. The production cross sections for the d-induced reactions are larger in the small ΔZ region than are those of the p-induced reactions. Since incident deuterons have twice the kinetic energy of protons, the prefragments generated via the INC stage have higher excitation energies than those produced by p-induced reactions. The higher excitation energy allows the prefragments to emit more particles, including protons, in the evaporation stage. Thus, it is expected that the distributions is shifted to lower ΔZ. In addition, the neutron contained in the deuteron may affect the shift of the distribution to low ΔZ in the d-induced reactions. Since the n-p scattering cross section is larger than the p-p scattering one, an incident deuteron is more likely to knock out protons of a target nucleus in the INC process than is an the incident proton. As a result, the ΔZ distributions of the d-induced reactions are broader than the p-induced ones in both of the ^{93}Nb and ^{93}Zr data.

V. SUMMARY AND CONCLUSIONS

The isotope-production cross sections in p-, d-, and C-induced reactions on ^{93}Nb at 113 MeV/nucleon were measured by using the inverse-kinematics method. The measured data were compared with the available activation data, the theoretical calculations by the reaction models implemented in Particle and Heavy Ion Transport code System (PHITS), and the latest nuclear data libraries (JENDL-4.0/HE, TENDL-2017, and ENDF/B-VIII.0). Moreover, the p- and d-induced production cross sections on ^{93}Nb were compared with the data of ^{93}Zr, that is one of LLFPs and a neighboring isobar of ^{93}Nb, in order to investigate how the neutron shell closure with the magic number 50 affects the isotopic distribution of production cross sections.

First, we found that within the experimental uncertainties the measured production cross sections for ^{90}Mo, ^{90}Nb, and ^{86,88}Y produced by p-induced reactions on ^{93}Nb are in fairly good agreement with those measured by the activation method. This confirms the consistency between the isotope-production cross sections measured by the two

different methods. It should be emphasized that the inverse-kinematics method is suitable for the investigation of isotope production over a wide range of mass numbers, including stable isotopes, compared with the conventional activation method.

Second, we benchmarked the reaction models implemented in PHITS and the nuclear data libraries by comparisons with the measured isotope-production cross sections. The model calculations with INCL-4.6 + GEM showed generally good agreement with the experimental data for the p- and d-induced reactions, although some discrepancies were seen, e.g., the overestimate of ^{92}Mo production and the exaggerated even-odd staggering in the calculated isotopic distributions. Noticeable jumps seen in the measured production cross sections for ^{90}Zr and ^{91}Zr were reproduced by the PHITS calculations reasonably well. For the C-induced reactions on ^{93}Nb, we compared model calculations using both JQMD + GEM and JQMD-2.0 + GEM with the measured data. The underestimate of ^{91,92}Nb seen in the JQMD + GEM calculation was considerably improved in the JQMD-2.0 + GEM calculations due to the improved treatment of peripheral collisions in JQMD-2.0. However, neither calculation reproduced very well the charge-exchange reaction leading to the production of Mo isotopes. From comparisons with the three nuclear data libraries, we found that JENDL-4.0/HE is in better agreement with the experimental data than TENDL-2017 or ENDF/B-VIII.0.

Third, we compared the measured ^{93}Nb data to the ^{93}Zr data, with particular attention to the effect of neutron-shell closure on the isotopic distribution of production cross sections. We observed noticeable jumps at the neutron number $N = 50$ in the Zr and Y isotopes produced by the p- and d-induced reactions on ^{93}Zr. In contrast, although such a jump was clearly seen at $N = 50$ in the Zr isotopes produced by the p- and d-induced reactions on ^{93}Nb, it disappeared in the Nb isotopes produced by the same reactions. Our INCL-4.6 + GEM calculations showed that the isotopes with removal neutron numbers $\Delta N = 1$ and 2 are produced mainly by the INC process, whereas the jump at $N = 50$ appears in the isotopic distribution formed by evaporation from the excited prefragments generated by the INC process. This indicates that the appearance of the jump in the isotopic distribution depends on the relative fractions of the INC and evaporation components in the isotope production. We have thus clarified that the jump formed in the evaporation process is smeared out by the INC component in the production of ^{91}Nb by the $(p, p2n)$ and $(d, d2n)$ reactions on ^{93}Nb. Moreover, we compared the production cross sections obtained as a functions of the change in atomic number ΔZ (i.e., the removal number of protons) for the p- and d-induced reactions on ^{93}Nb and ^{93}Zr. The ΔZ distributions showed that the production cross sections with $\Delta Z = 0$ for ^{93}Nb are smaller than those for ^{93}Zr for both the p- and d-induced reactions, whereas those with $\Delta Z = 1$ for ^{93}Nb are larger than those for ^{93}Zr. These differences can be explained by the difference in the proton and neutron separation energies of the Zr and Nb isotopes. That is, the proton-separation energies of the Nb isotopes with $Z = 41$ are much smaller than those of the Zr isotopes with $Z = 40$, resulting predominantly in proton emission from the excited Nb isotopes generated by the INC process.

Finally, secondary beams containing other isotopes near the neutron magic number $N = 50$ (i.e., ^{91,92}Y, ^{92}Zr, and ^{94}Nb) at kinetic energies around 100 MeV/nucleon were also produced in this inverse-kinematics experiment by the in-flight fission of ^{238}U at 345 MeV/nucleon after passing through a beryllium target. It will therefore be possible to obtain systematic data for the isotope-production cross sections of p- and d-induced spallation reactions by the same method of data analysis as used in the present work. As a result, in the future, such systematic data will be able to contribute to further study of the effects of shell closure on p- and d-induced spallation reactions.

ACKNOWLEDGMENTS

We would like to thank the accelerator staff of the RIKEN Nishina Center for providing a high-quality ^{238}U primary beam. This work was funded by ImPACT Program of Council for Science, Technology and Innovation (Cabinet Office, Government of Japan).

[1] Y. Blumenfeld, T. Nilsson, and P. V. Duppen, Phys. Scr., T **152**, 014023 (2013).
[2] C. D. Bowman, Annu. Rev. Nucl. Part. Sci. **48**, 505 (1998).
[3] F. Maekawa, M. Harada, K. Oikawa, M. Teshigawara, T. Kai, S. Meigo, M. Ooi, S. Sakamoto, H. Takada, M. Futakawa, T. Kato, Y. Ikeda, N. Watanabe, T. Kamiyama, S. Torii, R. Kajimoto, and M. Nakamura, Nucl. Instrum. Methods Phys. Res., Sect. A **620**, 159 (2010).
[4] M. Gloris, R. Michel, F. Sudbrock, U. Herpers, P. Malmborg, and B. Holmqvist, Nucl. Instrum. Methods Phys. Res., Sect. A **463**, 593 (2001).
[5] Y. E. Titarenko, O. V. Shvedov, V. F. Batyaev, E. I. Karpikhin, V. M. Zhivun, A. B. Koldobsky, R. D. Mulambetov, S. V. Kvasova, A. N. Sosnin, S. G. Mashnik, R. E. Prael, A. J. Sierk, T. A. Gabriel, M. Saito, and H. Yasuda, Phys. Rev. C **65**, 064610 (2002).
[6] G. D. Westfall, T. J. M. Symons, D. E. Greiner, H. H. Heckman, P. J. Lindstrom, J. Mahoney, A. C. Shotter, D. K. Scott, H. J. Crawford, C. McParland, T. C. Awes, C. K. Gelbke, and J. M. Kidd, Phys. Rev. Lett. **43**, 1859 (1979).
[7] W. R. Webber, J. C. Kish, and D. A. Schrier, Phys. Rev. C **41**, 547 (1990).
[8] P. Armbruster, J. Benlliure, M. Bernas, A. Boudard, E. Casarejos, S. Czajkowski, T. Enqvist, S. Leray, P. Napolitani, J. Pereira, F. Rejmund, M.-V. Ricciardi, K.-H. Schmidt, C. Stéphan, J. Taieb, L. Tassan-Got, and C. Volant, Phys. Rev. Lett. **93**, 212701 (2004).
[9] W. Wlazło, T. Enqvist, P. Armbruster, J. Benlliure, M. Bernas, A. Boudard, S. Czájkowski, R. Legrain, S. Leray, B. Mustapha, M. Pravikoff, F. Rejmund, K.-H. Schmidt, C. Stéphan, J. Taieb, L. Tassan-Got, and C. Volant, Phys. Rev. Lett. **84**, 5736 (2000).

[10] J. Benlliure, M. Fernández-Ordóñez, L. Audouin, A. Boudard, E. Casarejos, J. E. Ducret, T. Enqvist, A. Heinz, D. Henzlova, V. Henzl, A. Kelic, S. Leray, P. Napolitani, J. Pereira, F. Rejmund, M. V. Ricciardi, K.-H. Schmidt, C. Schmitt, C. Stéphan, L. Tassan-Got *et al.*, Phys. Rev. C **78**, 054605 (2008).

[11] D. Pérez-Loureiro, J. Benlliure, H. Álvarez-Pol, B. Blank, E. Casarejos, D. Dragosavac, V. Föhr, M. Gascón, W. Gawlikowicz, A. Heinz, K. Helariutta, A. Kelić-Heil, S. Lukić, F. Montes, L. Pieńkowski, K.-H. Schmidt, M. Staniou, K. Subotić, K. Sümmerer, J. Taieb *et al.*, Phys. Lett. B **703**, 552 (2011).

[12] S. Kawase, K. Nakano, Y. Watanabe, H. Wang, H. Otsu, H. Sakurai, D. S. Ahn, M. Aikawa, T. Ando, S. Araki, S. Chen, N. Chiga, P. Doornenbal, N. Fukuda, T. Isobe, S. Kawakami, T. Kin, Y. Kondo, S. Koyama, S. Kubono *et al.*, Prog. Theor. Exp. Phys. **2017**, 093D03 (2017).

[13] H. Wang, H. Otsu, H. Sakurai, D. S. Ahn, M. Aikawa, T. Ando, S. Araki, S. Chen, C. Nobuyuki, P. Doornenbal, N. Fukuda, T. Isobe, S. Kawakami, S. Kawase, T. Kin, Y. Kondo, S. Koyama, S. Kubono, Y. Maeda, A. Makinaga *et al.*, Prog. Theor. Exp. Phys. **2017**, 021D01 (2017).

[14] Y. E. Titarenko, V. F. Batyaev, A. Y. Titarenko, M. A. Butko, K. V. Pavlov, S. N. Florya, R. S. Tikhonov, V. M. Zhivun, A. V. Ignatyuk, S. G. Mashnik, S. Leray, A. Boudard, J. Cugnon, D. Mancusi, Y. Yariv, K. Nishihara, N. Matsuda, H. Kumawat, G. Mank, and W. Gudowski, Phys. At. Nucl. **74**, 537 (2011).

[15] K. Shibata, O. Iwamoto, T. Nakagawa, N. Iwamoto, A. Ichihara, S. Kunieda, S. Chiba, K. Furutaka, N. Otuka, T. Ohasawa, T. Murata, H. Matsunobu, A. Zukeran, S. Kamada, and J. Katakura, J. Nucl. Sci. Technol. **48**, 1 (2011).

[16] A. Koning and D. Rochman, Nucl. Data Sheets **113**, 2841 (2012).

[17] D. Brown, M. Chadwick, R. Capote, A. Kahler, A. Trkov, M. Herman, A. Sonzogni, Y. Danon, A. Carlson, M. Dunn, D. Smith, G. Hale, G. Arbanas, R. Arcilla, C. Bates, B. Beck, B. Becker, F. Brown, R. Casperson, J. Conlin *et al.*, Nucl. Data Sheets **148**, 1 (2018).

[18] A. Boudard, J. Cugnon, J.-C. David, S. Leray, and D. Mancusi, Phys. Rev. C **87**, 014606 (2013).

[19] S. Furihata, Nucl. Instrum. Methods Phys. Res., Sect. B **171**, 251 (2000).

[20] T. Sato, Y. Iwamoto, S. Hashimoto, T. Ogawa, T. Furuta, S. Abe, T. Kai, P.-E. Tsai, N. Matsuda, H. Iwase, N. Shigyo, L. Sihver, and K. Niita, J. Nucl. Sci. Technol. **55**, 684 (2018).

[21] Y. Iwamoto, T. Sato, S. Hashimoto, T. Ogawa, T. Furuta, S. Abe, T. Kai, N. Matsuda, R. Hosoyamada, and K. Niita, J. Nucl. Sci. Technol. **54**, 617 (2017).

[22] K. Niita, S. Chiba, T. Maruyama, T. Maruyama, H. Takada, T. Fukahori, Y. Nakahara, and A. Iwamoto, Phys. Rev. C **52**, 2620 (1995).

[23] T. Ogawa, T. Sato, S. Hashimoto, D. Satoh, S. Tsuda, and K. Niita, Phys. Rev. C **92**, 024614 (2015).

[24] T. Kubo, D. Kameda, H. Suzuki, N. Fukuda, H. Takeda, Y. Yanagisawa, M. Ohtake, K. Kusaka, K. Yoshida, N. Inabe, T. Ohnishi, A. Yoshida, K. Tanaka, and Y. Mizoi, Prog. Theor. Exp. Phys. **2012**, 03C003 (2012).

[25] N. Fukuda, T. Kubo, T. Ohnishi, N. Inabe, H. Takeda, D. Kameda, and H. Suzuki, Nucl. Instrum. Methods Phys. Res., Sect. B **317**, 323 (2013).

[26] C. M. Folden, A. S. Nettleton, A. M. Amthor, T. N. Ginter, M. Hausmann, T. Kubo, W. Loveland, S. L. Manikonda, D. J. Morrissey, T. Nakao, M. Portillo, B. M. Sherrill, G. A. Souliotis, B. F. Strong, H. Takeda, and O. B. Tarasov, Phys. Rev. C **79**, 064318 (2009).

[27] T. Ohnishi, T. Kubo, K. Kusaka, A. Yoshida, K. Yoshida, M. Ohtake, N. Fukuda, H. Takeda, D. Kameda, K. Tanaka, N. Inabe, Y. Yanagisawa, Y. Gono, H. Watanabe, H. Otsu, H. Baba, T. Ichihara, Y. Yamaguchi, M. Takechi, S. Nishimura *et al.*, J. Phys. Soc. Jpn. **79**, 073201 (2010).

[28] T. Ohnishi, T. Kubo, K. Kusaka, A. Yoshida, K. Yoshida, N. Fukuda, M. Ohtake, Y. Yanagisawa, H. Takeda, D. Kameda, Y. Yamaguchi, N. Aoi, K.-i. Yoneda, H. Otsu, S. Takeuchi, T. Sugimoto, Y. Kondo, H. Scheit, Y. Gono, H. Sakurai *et al.*, J. Phys. Soc. Jpn. **77**, 083201 (2008).

[29] O. Iwamoto, N. Iwamoto, S. Kunieda, F. Minato, and K. Shibata, Nucl. Data Sheets **131**, 259 (2016).

[30] O. Tarasov and D. Bazin, Nucl. Instrum. Methods Phys. Res., Sect. B **376**, 185 (2016).

[31] H. Wang, H. Otsu, H. Sakurai, D. S. Ahn, M. Aikawa, P. Doornenbal, N. Fukuda, T. Isobe, S. Kawakami, S. Koyama, T. Kubo, S. Kubono, G. Lorusso, Y. Maeda, A. Makinaga, S. Momiyama, K. Nakano, M. Niikura, Y. Shiga, P.-A. Söderström *et al.*, Phys. Lett. B **754**, 104 (2016).

[32] J. Alcántara-Núñez, J. Benlliure, C. Paradela, C. Pérez-Loureiro, J. L. Rodríguez-Sánchez, L. Audouin, A. Boudard, E. Casarejos, T. Enqvist, F. Farget, M. Fernández-Ordóñez, A. Heinz, V. Henzl, D. Henzlova, A. Kelić-Heil, A. Lafriaskh, S. Leray, P. Napolitani, J. Pereira, M. V. Ricciardi *et al.*, Phys. Rev. C **92**, 024607 (2015).

[33] M. Wang, G. Audi, F. G. Kondev, W. Huang, S. Naimi, and X. Xu, Chin. Phys. C **41**, 030003 (2017).

[34] K. Niita, H. Takada, S. Meigo, and Y. Ikeda, Nucl. Instrum. Methods Phys. Res., Sect. B **184**, 406 (2001).

[35] L. Sihver, A. Kohama, K. Iida, K. Oyamatsu, S. Hashimoto, H. Iwase, and K. Niita, Nucl. Instrum. Methods Phys. Res., Sect. B **334**, 34 (2014).

[36] K. Iida, A. Kohama, and K. Oyamatsu, J. Phys. Soc. Jpn. **76**, 044201 (2007).

[37] D. Mancusi, A. Boudard, J. Carbonell, J. Cugnon, J.-C. David, and S. Leray, Phys. Rev. C **91**, 034602 (2015).

[38] J. L. Rodríguez-Sánchez, J.-C. David, D. Mancusi, A. Boudard, J. Cugnon, and S. Leray, Phys. Rev. C **96**, 054602 (2017).